ACS OMEGA

Open Access

http://pubs.acs.org/journal/acsodf

Article

First-Principles Calculations on Electronic, Optical, and Phonon Properties of γ-Bi_2MoO_6

Shahad Saroar, Shadmin Sultana, Sadiq Shahriyar Nishat, Quazi Shafayat Hossain, M. N. I. Khan, Dipa Islam, Umme Sarmeen Akhtar, Muhammad Shahriar Bashar, Sharmin Jahan, Khandker Saadat Hossain, and Imtiaz Ahmed*

Cite This: *ACS Omega* 2024, 9, 36314−36325

Read Online

ACCESS | Metrics & More | Article Recommendations | Supporting Information

ABSTRACT: The wide band gap γ-Bi_2MoO_6 (BMO) has tremendous potential in emergent solar harvesting applications. Here we present a combined experimental−first-principles density functional theory (DFT) approach to probe physical properties relevant to the light sensitivity of BMO like dynamic and structural stability, Raman and infrared absorption modes, value and nature of band gap (i.e., direct or indirect), dielectric constant, and optical absorption, etc. We solvothermally synthesized wide band gap $Pca2_1$ phase pure BMO ($\gtrsim$3 eV) for two different pH values of 7 and 9. The structural parameters were correlated with the stability of BMO derived from elastic tensor simulations. The desired dynamical stability at T = 0 K was established from the phonon vibrational band structure using a finite difference-based supercell approach. The DFT-based Raman modes and phonon density of states (DOS) reliably reproduced the experimental Raman and infrared absorption. The electronic DOS calculated from Heyd−Scuseria−Ernzerhof HSE06 with van der Waals (vdW) and relativistic spin−orbit coupling (SOC) corrections produced a good agreement with the band gap obtained from diffuse reflectance spectroscopy (DRS). The optical absorption obtained from the complex dielectric constant for the HSE06+SOC+vdW potential closely resembled the DRS-derived absorption of BMO. The BMO shows ∼43% photocatalytic efficiency in degrading methylene blue dye under 75 min optical illumination. This combined DFT-experimental approach may provide a better understanding of the properties of BMO relevant to solar harvesting applications.

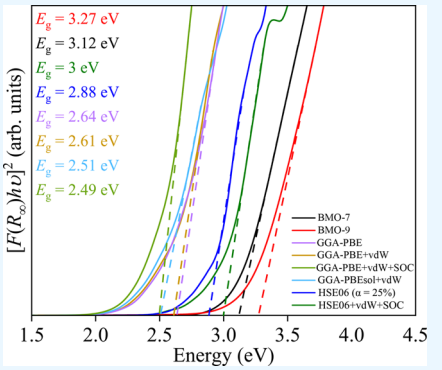

1. INTRODUCTION

The semiconductor ternary oxide bismuth molybdates have been at the forefront of research due to their potential in solar harvesting applications such as photocatalytic pollutant degradation, hydrogen evolution, photocatalytic oxidation, energy storage, gas sensing, luminescence, and dielectric applications.[1−12] Their functional behavior relevant to light-sensitive applications is governed by fundamental properties like the value and nature of the band gap (i.e., direct or indirect), dielectric constant, optical absorption, and the presence of a particular phase.[13] It exists in three different phases with a general chemical structure of $Bi_2O_3{\cdot}nMoO_3$, where n = 3, 2, and 1 correspond to α-$Bi_2Mo_3O_{12}$ (monoclinic), β-$Bi_2Mo_2O_9$ (monoclinic), and γ-Bi_2MoO_6 (orthorhombic), respectively.[14−16] Out of these three polymorphs, the γ-Bi_2MoO_6 (BMO) phase consisting of $[Bi_2O_2]^{2+}$ layers in the Aurivillius perovskite structure sandwiched with corner-sharing distorted MoO_6 octahedral units displayed the best photocatalytic behavior. The distinguished photocatalytic properties in BMO can be attributed to spin−orbit coupling (SOC), sp coupling, lone-pair, and the stereochemical activity of bismuth.[17−21] The presence of Bi^{3+} and Mo^{6+} ions also provides chemical stability and suitable valence band potential in BMO.[22,23] Moreover, both the structural and the dynamic stability of BMO are crucial for photosensitive applications.

BMO was synthesized using various techniques, including solid-state reaction, hydrothermal, solvothermal, coprecipitation, and solution combustion.[24−27] The presence of polymorphism complicates the orthorhombic phase purity during synthesis. In the energy-friendly low-temperature solvothermal method, precise pH control is crucial for obtaining phase purity. Moreover, properties such as band gap and optical absorption coefficients depend on the pH values during the synthesis, morphology, crystallinity, and texture of BMO.[28] Attempts have been made to probe the functional properties of BMO based on ab initio density functional theory (DFT). The use of the generalized gradient approximation of the Perdew−Burke−Ernzerhof (GGA-PBE) exchange-correlation functional produced underestimation of the band gap E_g = 1.53 eV.[29] The

Received: April 2, 2024
Revised: June 28, 2024
Accepted: July 5, 2024
Published: August 14, 2024

https://doi.org/10.1021/acsomega.4c03171
ACS Omega 2024, 9, 36314−36325

modified Becke−Johnson functional improved the E_g estimation to ∼2.4 eV.[30] A similar E_g value of 2.43 eV was obtained using GGA-PBE with scissor corrections.[31] Several challenges to model BMO with a wider $E_g \gtrsim 3$ can be envisioned. The binding energy underestimation of localized d orbitals in Bi can inflate its hybridization with p orbitals.[32−37] This spurious p−d coupling enhancement may shift the valence band maximum up in energy, leading to band gap narrowing effects.[38] Moreover, the Mo-4d orbitals in BMO are less spatially localized than the 3d orbitals present in many other transition metals.[39] This can make the Hubbard interaction U corrections less effective in tuning the electronic properties of BMO within the DFT+U approach.[40] The inherent lattice parameter overestimation problem due to the self-interaction error in GGA-PBE may require the van der Waals (vdW) force to be included.[37] Computationally intensive hybrid functionals may become necessary for reliable electronic and optical property simulations. Moreover, heavy metals like Bi can impose relativistic SOC corrections that should be included in the model. It is crucial to address these issues during reliable modeling of the physical properties like band gap, optical absorption, Raman and infrared absorption, dielectric constant, and structural and dynamic stability of BMO relevant to light-sensitive applications.

Herein, we solvothermally synthesized the $Pca2_1$ phase pure wide band gap BMO for two pH values of 7 and 9. We correlated the structural parameters with the elastic properties via the equation of state based on energy versus volume relaxation and elastic tensor simulations. The experimentally observed Raman and infrared absorptions were modeled with Raman tensor and phonon density of states (DOS) simulations. The essential dynamical stability of BMO at T = 0 K was established from the phonon band structure (BS) along different high symmetry points in the Brillouin zone (BZ). The surface morphology, elemental identification, and chemical states of BMO were investigated with field emission scanning electron microscopy, energy dispersive X-ray spectroscopy, and X-ray photoelectron spectroscopy, respectively. The complex dielectric constant was calculated for several different exchange-correlation (xc) functionals to probe the linear optical properties of BMO. The incorporation of relativistic SOC and vdW corrections to the Heyd−Scuseria−Ernzerhof hybrid functional with Hartree−Fock exact-exchange mixing α_{HF} = 25% validated the optical absorption and direct nature of the electronic band gap, along with its magnitude obtained from diffuse reflectance spectroscopy (DRS). The photocatalytic methylene blue (MB) dye degradation performance of BMO was characterized by UV−vis absorption spectroscopy. Overall, this combined experimental-DFT approach may have successfully probed the physical properties of BMO relevant to solar harvesting applications.

2. METHODOLOGY

2.1. Computational Details. The Vienna Ab Initio Simulation Package VASP 6.1.0 code was used to obtain spin-polarized DFT-based simulations where core−valence interactions were modeled with the projector-augmented wave (PAW) method.[41−43] The pure orthorhombic γ-Bi_2MoO_6 unit cell is comprised of 36 atoms consisting of Bi (8), Mo (4), and O (24) as constituent elements. The $5d^{10}6s^26p^3$ for Bi, $4s^25s^14p^64d^5$ for Mo, and $2s^22p^4$ for O were considered as valence electrons in the PAW. For volume and structural relaxations, the electronic eigenstates were represented by plane wave expansion with an energy cutoff of 620 eV, 10^{-4} eV/Å for Hellmann−Feynman force, and 10^{-8} eV/atom for self-consistent total energy convergences, respectively. The Brillouin zone (BZ) integrations were performed with 9 × 3 × 9 Monkhorst−Pack k-mesh.

The accuracy of DFT simulation is linked with the computational complexity of the xc functional.[44,45] Several different functionals like Local Density Approximation (LDA), GGA-PBE, GGA-PBE for solid (GGA-PBEsol), and the Hubbard U corrected GGA-PBE+U_d+U_p, sharing similar computational cost, were considered to approximate the electron xc interactions.[46−53] The sophisticated Heyd−Scuseria−Ernzerhof (HSE06) with 25% Hartree−Fock (HF) α_{HF} exact-exchange mixing was also implemented.[13,32,34,54−58] The vdW force was included by DFT-D3 equipped with Becke−Johnson (BJ) damping.[59] The relativistic effect of Bi was incorporated by considering the SOC.[60] The vdW and SOC corrections were included with different xc functionals to implement GGA-PBE+vdW, GGA-PBEsol+vdW, GGA-PBE +vdW+SOC, HSE06+vdW, and HSE06+vdW+SOC.

The equation of state (EOS)-based bulk modulus and elastic properties from elastic tensor simulations were performed at the GGA-PBE, GGA-PBE+vdW, and GGA-PBEsol+vdW levels with an increased plane wave cutoff of 680 eV to ensure reliable convergence of the stress tensor. The density functional perturbation theory (DFPT) was first employed to probe the phonon DOS and BS with nonanalytical corrections turned off and on.[61,62] The phonon vibrational spectrum was further probed with varying supercell sizes using a finite difference approach in Phonopy 2.22.1 where the second-order force constants were obtained with GGA-PBE+vdW and GGA-PBEsol+vdW.[62−64] The electronic properties were probed with various xc approximations like GGA-PBE, GGA-PBE+vdW, GGA-PBE+vdW+SOC, and GGA-PBE+U_d+U_p. The U corrections have been applied to Bi-6p, Bi-5d, Mo-4d, and O-2p orbitals within the GGA-PBE+U_d+U_p approach.[50−53] Several U_p (15, 18, and 21 eV) and U_d (5 and 15 eV) values were applied on Bi-6p and Bi-5d, respectively. Two different U_d = 5 and 15 eV were used on Mo-4d. In the case of O-2p, the U_p values of 5 and 15 eV were considered. For a more accurate account of electronic properties, HSE06, HSE06+vdW, and HSE06+vdW+SOC were invoked.[13,32,34,54−58,60] The electronic BS simulations based on HSE06, HSE06+vdW, and HSE06+vdW+SOC were kept tractable with Wannier interpolation using the WANNIER90 tool.[32,35,65,66] The complex dielectric constant calculations for various xc approximations were used to characterize the optical absorptions.

The Raman mode calculations were done in QUANTUM-ESPRESSO (QE 7.3.1) code with LDA and GGA-PBE potentials.[46,47,67−72] The Monkhorst Pack 9 × 3 × 9 grid k-points mesh was used to sample the BZ during the full structural relaxation and optimization until the Hellmann−Feynman force and self-consistent total electronic energy convergence thresholds reached 10^{-4} eV/Å and 10^{-8} eV/atom. The Raman tensor was derived from the calculated finite difference-based derivatives of the dielectric tensor with 0.01 Å atomic displacement with dynmat.x code in the QE package.[73,74]

2.2. Sample Preparation. *2.2.1. Solvothermal Synthesis-I.* The AR grade 0.5 mmol (0.243 g) of $Bi(NO_3)_3{\cdot}5H_2O$ and 0.5 mmol (0.121 g) of $Na_2MoO_4{\cdot}2H_2O$ precursors were

https://doi.org/10.1021/acsomega.4c03171
ACS Omega 2024, 9, 36314−36325

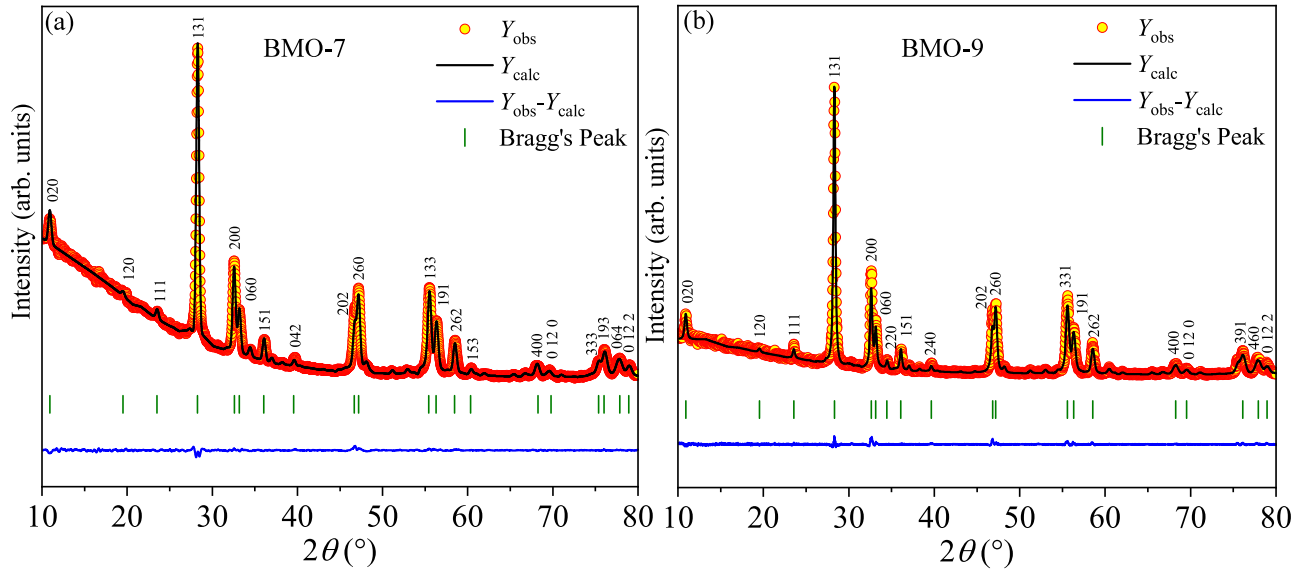

Figure 1. Rietveld refined powdered XRD data for (a) BMO-7 and (b) BMO-9. The yellow circles are the experimental data points (Y_{obs}), the black solid line represents the calculated refined pattern Y_{calc}, and the bottom blue curve shows the difference between the Y_{obs} and Y_{calc} values.

dissolved into a mixture of 20 mL of ethylene glycol and 10 mL of nanowater (18 MΩ) under vigorous magnetic stirring (550 rpm) for 45 min until a white cloudy solution was formed at pH = 7.[75] The solution was thermally reacted at 160 °C inside a 100 mL Teflon-lined autoclave for 18 h inside a universal oven. The solution was cooled to room temperature, and the resulting ashy precipitate was collected through centrifuging (7000 rpm), and washing with ethanol (3 cycles) and nanowater (3 cycles). The bright yellow sample was obtained by drying the product at 80 °C for 16 h before being sintered at 400 °C for 2 h. This sample was termed as BMO-7 hereafter.

2.2.2. Solvothermal Synthesis-II. In this approach, stoichiometric proportions of 5 mmol (2.43 g) of $Bi(NO_3)_3 \cdot 5H_2O$ and 0.38 mmol (0.441 g) of $(NH_4)_6Mo_7O_{24} \cdot 4H_2O$ were dissolved into 50 mL of ethylene glycol with magnetic stirring (650 rpm) for 1 h. The solution pH value was set to 9 with 5% NH_4OH solution.[26] The solvothermal reaction temperature was set to 180 °C for 24 h by loading the Teflon-lined autoclave inside the oven. The powdered sample labeled as BMO-9 was obtained after subsequent centrifugation, washing, and drying.

2.2.3. Photocatalytic Sample Preparation. The 10 ppm MB solution was prepared by dissolving the dye into 100 mL of nanowater. The BMO-7 and BMO-9 photocatalyst concentrations were set to 0.2 g/L. The NH_4OH solution was used to set the dye−photocatalyst mixture pH to 10. The required solution adsorption−desorption equilibrium was reached by constant and vigorous magnetic stirring for 30 min in the dark condition. A 100 W Hg−Xe lamp with a fused silica window was used as a sun simulator during the photocatalytic measurements performed at the ambient temperature of ∼300 K. During the optical exposure, constant magnetic stirring prevented the unwanted MB concentration gradients in the solution and ensured homogeneity to nullify the spurious degradation effects. The photocatalyst removal was facilitated by high-speed centrifugation before the subsequent UV−vis absorption spectra recording in periodic intervals of 30 (15) min over 180 (75) min duration for the BMO-7 (BMO-9) sample.

2.3. Characterization Techniques. The Nebertherm LT 5/14 and Kejia M1700 muffle furnaces were used to sinter the sample. The crystal structures were probed with powdered λ = 0.15418 nm Cu Kα X-ray diffraction (XRD) (tube voltage 40 kV, beam current 40 mA, step size 0.02°, scan speed 2°/min) from 10° to 80° using a Rigaku SmartLab SE multipurpose XRD system. The Horiba Scientific Confocal Raman microscope LabRAM HR Evolution with 532 nm laser was used to extract the room-temperature Raman modes. The characteristic infrared absorptions were obtained using a PerkinElmer Fourier transform infrared (FTIR) spectrometer. Surface morphology, elemental identification, and purity analysis were performed with a field emission scanning electron microscope (FESEM, JEOL 7610F) coupled with EDX (model: JED 2300). The elemental binding energies were acquired using a 1486.69 eV Al Kα source at 225 W in a Thermo Fischer Scientific X-ray photoelectron spectrometer. The binding energy calibration was done by shifting the C-1s X-ray photoelectron spectroscopy (XPS) peak to 284.8 eV. UV−vis diffuse reflectance spectroscopy (DRS) was carried out with a Shimadzu UV-2600i UV−vis−NIR spectrometer. The UV−vis absorption measurements during photocatalytic degradation were done with a Shimadzu UV-1900i spectrometer.

3. RESULTS AND DISCUSSION

3.1. XRD Analysis and Equation of State. The Rietveld refined powder XRD patterns of BMO-7 and BMO-9 were shown in Figure 1a,b, respectively. The experimental crystallographic parameters were derived from refinement and recorded in Table S1. The XRD peaks of both BMO-7 and BMO-9 were indexed as phase pure orthorhombic koechlinite BMO (JCPDS 21-0102, space group $Pca2_1$) with the Rietveld factors [R_{wp} = 6.35%, R_{exp} = 5.08%, χ^2 = 1.56] and [R_{wp} = 6.58%, R_{exp} = 5.46%, χ^2 = 1.45], respectively.[14,15,29,76] The lattice parameters were estimated to be a = 5.4901(2), b = 16.1973(2), and c = 5.5072(3) Å [a = 5.4852(2), b = 16.2182(1), and c = 5.5011(2) Å] for BMO-7 (BMO-9) from the Rietveld refinement. The desired (020), (120), (111), (131), (200), (060), (151), (042), (202), (260), (133), and

https://doi.org/10.1021/acsomega.4c03171
ACS Omega 2024, 9, 36314−36325

(191) Miller planes for both samples were located at correct diffraction angles. The sharp and intense peaks corroborate the crystallinity of the as-synthesized samples. No impurity peaks were present in the XRD data.

The summary of DFT simulated crystallographic information was also presented in Table S1. The BMO-7 and BMO-9 have the same γ-Bi_2MoO_6 crystallographic structure. All DFT simulations presented here are based on the unit cell of the orthorhombic γ-Bi_2MoO_6. The GGA-PBE overestimated the unit cell volume (530.8645(4) Å^3) due to a well-known self-interaction problem.[77,78] The volume overestimation was reduced to 499.8724(3) Å^3 by incorporating the vdW force as GGA-PBE+vdW.[37] In the case of GGA-PBEsol+vdW, the vdW force inclusion underestimated the unit cell volume to 467.0268(4) Å^3 due to overbinding the atoms in the unit cell. The Hubbard corrections U_d and U_p often produced crystallographic overestimation problems in GGA-PBE $+U_d+U_p$.[36,37] Hence, the vdW corrections were used to reduce the volume estimation error in GGA-PBE$+U_d+U_p$+vdW.

To correlate the structural and elastic properties, structural optimization under zero pressure was performed for GGA-PBE, GGA-PBE+vdW, and GGA-PBEsol+vdW. The crystallographic parameters at minimum energy were recorded in Table S2. The energy (E) versus volume (V) curves in Figure 2

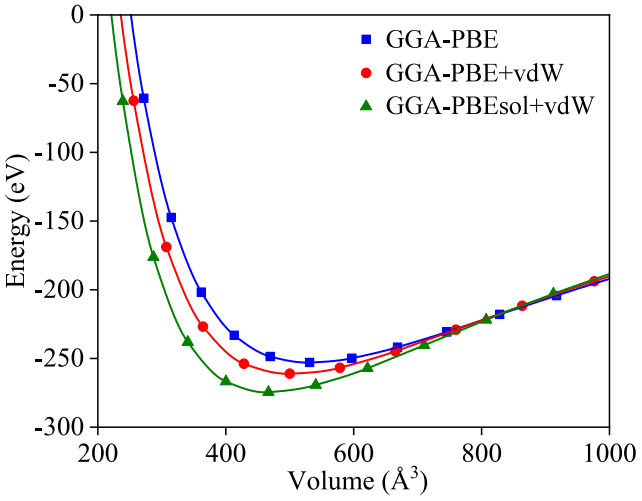

Figure 2. Energy versus volume of BMO for the GGA-PBE, GGA-PBE+vdW, and GGA-PBEsol+vdW functionals.

corroborate the volume reduction due to vdW corrections. The bulk modulus and its derivative were estimated from the third-order Birch–Murnaghan EOS using the minimum energy of the E versus V curve.[79,80] The simulated volume at minimum energy (V_0), bulk modulus (B_0), and its first pressure derivative (B_0') are collected in Table S2. The V_0 gradually decreases with the vdW corrections, which provide attractive forces between atoms of the unit cell. The vdW corrections inflate the compressibility by increasing the B_0.

3.2. Elastic Tensor Simulation. The mechanical stability of BMO was probed from the elastic properties (E.P.) simulations based on elastic tensor C_{ij}. By recording the response after applying perturbing forces in different directions of the unit cell, the C_{ij} tensor was obtained.[81,82] The convergence of the C_{ij} tensor was ensured by using a 680 eV plane wave energy cutoff. The six nonzero elastic constants C_{11}, C_{12}, C_{13}, C_{22}, C_{23}, C_{33}, C_{44}, C_{55}, and C_{66} of the orthorhombic BMO were simulated with GGA-PBE, GGA-PBE+vdW, and GGA-PBEsol+vdW potentials and displayed in Table S3. The Born criteria of mechanical stability

$$C_{11} > 0,\ C_{44} > 0,\ C_{55} > 0,\ C_{66} > 0,\ C_{11}C_{22} > C_{12}^2 \quad (1)$$

$$C_{11}C_{22}C_{33} + 2C_{12}C_{13}C_{23} - C_{11}C_{23}^2 - C_{22}C_{13}^2 - C_{33}C_{12}^2 > 0 \quad (2)$$

were fulfilled, ensuring the structural stability of the BMO.[83] The six stiffness eigenvalues λ_i (i = 1, ..., 6) turned out to be positive at ambient pressure. The pertinent elastic properties like bulk modulus (B), shear modulus (G), Young's modulus (E), Poisson's ratio (ν), and Pugh's ratio (k_{Pugh}) were calculated in the Voigt (V), Reuss (R), and Hill (H) frameworks.[84−86] The 44−62 GPa values of B_V, B_R, and B_H imply moderate incompressibility of BMO. These bulk moduli obtained from the elastic constant agree well with bulk modulus B_0 calculated from EOS, which validates the consistency of the simulations. The shear moduli G_V, G_R, and G_H values of 28−56 GPa favor the shear deformation over volume contraction. The Young's moduli E_V, E_R, and E_H lie in the range 68−128 GPa, which indicates large tensile (compressive) stiffness of BMO in response to force applied along the length. The vdW correction inflates the B, G, and E as it corrects the volume overestimation. Notably, B and G were smaller than E of BMO. This indicates a large tensile (or compressive) stiffness in response to lengthwise applied force.[80] Moreover, the B is larger than G, which implies BMO is susceptible to nonhydrostatic stress as shear deformations dominate over volume contraction. The brittle nature of BMO is evident as the Poisson's ratio lies below the threshold value of 0.33. The Pugh's ratio k_{Pugh} stayed below the brittle/ductile threshold value of 1.75.

3.3. Raman Mode Analysis. The deconvoluted room-temperature Raman spectra were presented in Figure 3. The

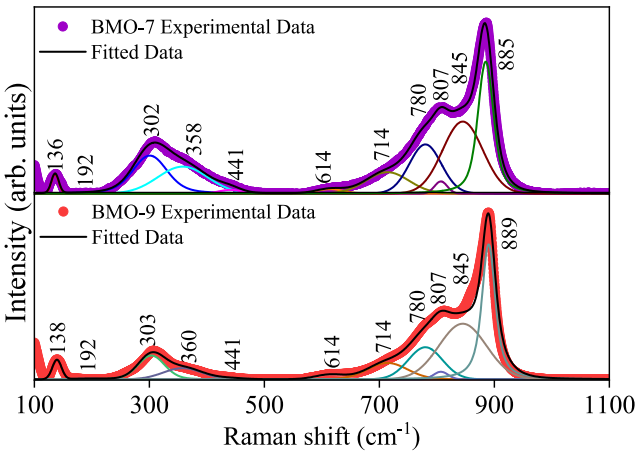

Figure 3. Deconvoluted room-temperature Raman spectra of BMO-7 and BMO-9.

detected nine Raman bands of both BMO-7 and BMO-9 can be identified by the irreducible representation $\Gamma_{Raman} = E_g + 4E_u + 2A_{1g} + A_{2u} + B_{1g}$ of the $Pca2_1$ group.[87−90] These Raman modes were in good agreement with refs 14, 27, 29, and 76. The DFT simulated Raman peaks using LDA and GGA-PBE potentials were benchmarked against the experimental observations in Table S4. The external lattice modes due to the translational motion of Bi and Mo atoms stemmed Raman

https://doi.org/10.1021/acsomega.4c03171
ACS Omega 2024, 9, 36314−36325

bands (E_g) at 136(2) and 192(2) cm^{-1}. The symmetric bending vibrations (E_u) of MoO_6 were located at 302(2), 358(2) (360(2)), and 441(2) cm^{-1}. The DFT-derived modes stayed within 1.3% of these modes. The MoO_6 octahedral symmetric stretching vibrations (E_u) were found at 614(2) and 714(2) cm^{-1}. The bands near 780(2) and 807(2) cm^{-1} were characteristic to symmetric stretching (A_{1g}) of MoO_6. The corresponding DFT-derived modes for all of these bands differ by less than 2.4%. The two Raman modes at 845(2) (A_{2u}) and 885(2) (889(2)) cm^{-1} marked the asymmetric stretching (B_{1g}) of Mo−O bonds. The relative difference with the DFT mode near ∼845 cm^{-1} is ∼2.72%. For the band near 885 cm^{-1}, the DFT simulated modes deviated by ∼6%. The LDA overbinds the atoms and tends to underestimate the atomic bonds in the unit cell. The GGA-PBE tends to underbind the atoms resulting in bond length overestimation. These bond length variations may have caused the discrepancies (≲6%) between simulation and experimental observations.

3.4. FTIR Absorption and Phonon Vibration Analysis. The FTIR bands of BMO-7 and BMO-9 as shown in Figure 4

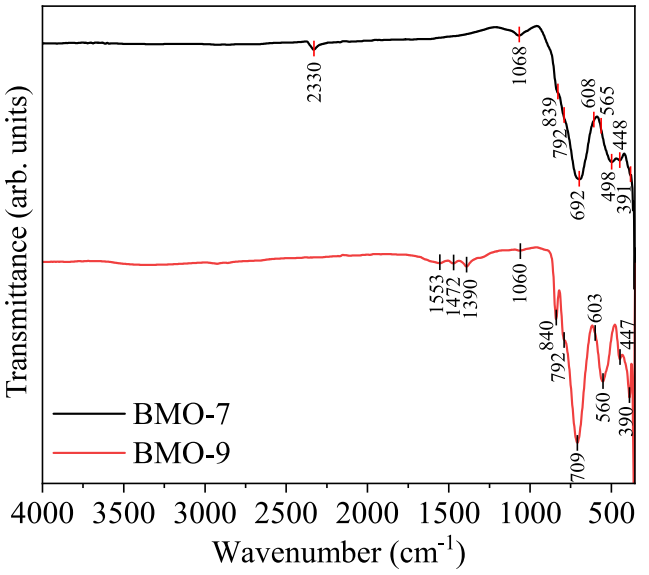

Figure 4. FTIR spectra of BMO-7 and BMO-9.

were recorded in Table S5. These bands have their origin in Bi−O and Mo−O/Mo−O−Bi bonds of Bi_2O_2 and MoO_6 units in the BMO crystal.[16,23,26,76,91] The FTIR bands at 390(4) and 448(4) cm^{-1} can be ascribed to symmetric stretching and bending vibrations of the Bi−O bonds. The bending vibration of O−Mo−O was located at 498(4) (516(4)) cm^{-1} in BMO-7 (BMO-9). The [MoO_6] octahedral bending motion stemmed from the IR absorption band near 565(4) and 608(4) cm^{-1}. The asymmetric stretching of [MoO_6] generated IR absorption situated at 692(4) (equatorial O) and 840(4) (apical O) cm^{-1}. The symmetric stretching of apical O in [MoO_6] appeared at 792 cm^{-1}. The band near 608(4) cm^{-1} represented the symmetric stretching of Mo−O. The symmetric stretching and bending of O−H in H_2O manifested itself at 1553 cm^{-1}. The C═O symmetric stretching in adsorbed CO_2 germinated 1390(4) and 1472(4) cm^{-1} bands in BMO-9, whereas its bending mode was located at 2330(4) cm^{-1} in BMO-7.

To probe the vibrational spectra in IR bands, the phonon BS and DOS of BMO were simulated using different techniques as shown in Figure S1. The DFPT method has successfully probed the dynamical stability of many different Bi-based oxide materials.[32−35] Yet in the case of the BMO, the imaginary modes were evident in DFPT-based phonon BS regardless of nonanalytic corrections in Figure S1a,b, respectively. This implied spurious dynamical instability of BMO at T = 0 K for DFPT with GGA-PBE+vdW potential. To eliminate these unwanted imaginary modes, a 2 × 1 × 2 supercell-based finite difference approach with both GGA-PBE+vdW and GGA-PBEsol+vdW potentials was used to simulate the phonon BS and DOS as shown in Figure 5a,b, respectively. The 3D (d = 3) BMO unit cell with n = 36 atoms possesses $d \times n$ = 108 phonon modes at the Γ point of the phonon BS. Out of these modes, three represent acoustic phonon and the remaining 105 modes characterize optical phonon. The three acoustic modes describe the translational motion of atoms as a whole and are degenerate at Γ-point. The absence of imaginary modes in the phonon BS corroborated the dynamical stability of BMO. The simulated DOS peak positions on the right column of Figure 5a,b matched well with the experimental FTIR peaks; see Table S5. The vibrations of atoms having heavy (Bi), moderate (Mo), and light (O) masses dominated over lower, moderate, and higher wavenumber ranges. The Born charge tensors calculated for GGA-PBE+vdW and GGA-PBEsol+vdW potentials with 2 × 1 × 2 supercells were displayed in Tables S8 and S10, respectively. The +4.74 (+4.80), +6.48 (+6.93), and −2.78 (−2.87) Born charges of Bi, Mo, and O for GGA-PBE+vdW (GGA-PBEsol+vdW) deviated from their closed shell values of +3, +6, and −2, respectively, due to the covalent nature of the bonding in BMO.

3.5. Surface Morphology and EDX Analysis. The FESEM micrographs of BMO-7 and BMO-9 were presented

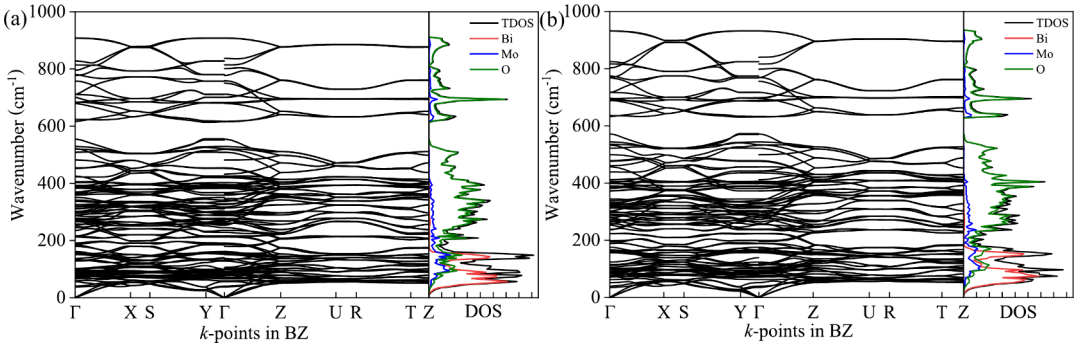

Figure 5. Phonon BS and DOS of BMO for (a) GGA-PBE+vdW and (b) GGA-PBEsol+vdW using the 2 × 1 × 2 supercell-based finite difference method. The phonon BS is simulated along the Γ, U, R, S, T, U, X, Y, Z high symmetry k-points in BZ.

https://doi.org/10.1021/acsomega.4c03171
ACS Omega 2024, 9, 36314−36325

in Figure 6a,b, respectively. The spherically shaped BMO-7 nanoparticles in Figure 6a were agglomerated due to inflated

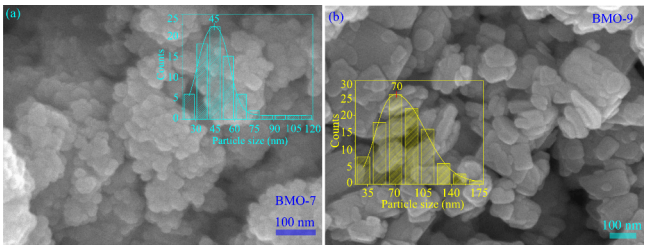

Figure 6. FESEM micrographs of (a) BMO-7 and (b) BMO-9 with particle size histograms superimposed.

surface energy common to hydrothermal methods. The histogram analysis revealed the average size of these nanoparticles to be ∼45 nm. The change in pH for BMO-9 promoted random rectangular pellet-like shapes in Figure 6b with an average size of ∼70 nm. The elemental identity and fraction of Bi, Mo, and O were examined using EDX; see Table S11. The experimental observations agreed quite well with the theoretical values regarding atomic percent (at. %) and weight percent (wt %) of Bi, Mo, and O. The EDX spectra of BMO-7 and BMO-9 in Figure S2 corroborated the elemental identifications for the Bi, Mo, and O atoms of BMO.

3.6. Chemical State Analysis. The presence of characteristic XPS peaks in the survey spectrum of BMO-9 in Figure 7a confirmed the existence of Bi, Mo, and O. The 5.3 eV spin−orbit splitting of the Bi-4$f_{7/2}$ and Bi-4$f_{5/2}$ XPS lines of Bi^{3+} in Figure 7b appeared at 159 and 164.3 eV, respectively. Meanwhile, the spin−orbit split of the Mo-3$d_{5/2}$ and Mo-3$d_{3/2}$ orbitals in Mo^{6+} cations stemmed the XPS peaks at 232.3 and 235.4 eV in Figure 7c, respectively. The origin of the XPS lines at 529.8 and 530.2 eV in Figure 7d can be explicated to O-1s of lattice O^{2-} in Bi−O and Mo−O, respectively. Moreover, the shoulder peak at 531.3 eV can be assigned to C═O in extraneous CO_2 present in the sample. Overall, the chemical states of Bi, Mo, and O were consistent with that of BMO in refs 29 and 92.

3.7. Optical Properties Analysis. The optical response of materials is encoded in the complex dielectric constant $\varepsilon(\omega) = \varepsilon_{real}(\omega) + i\varepsilon_{imag}(\omega)$, where ω stands for the angular frequency of the optical excitation. The imaginary part $\varepsilon_{imag}(\omega)$ was obtained from the dipole transition matrix. The real part $\varepsilon_{real}(\omega)$ was extracted from $\varepsilon_{imag}(\omega)$ using the Kramer−Kronig relation. Physically, $\varepsilon_{real}(\omega)$ models the electronic polarizability of the material.[93] Figure 8a represents ε_{real} of BMO for various

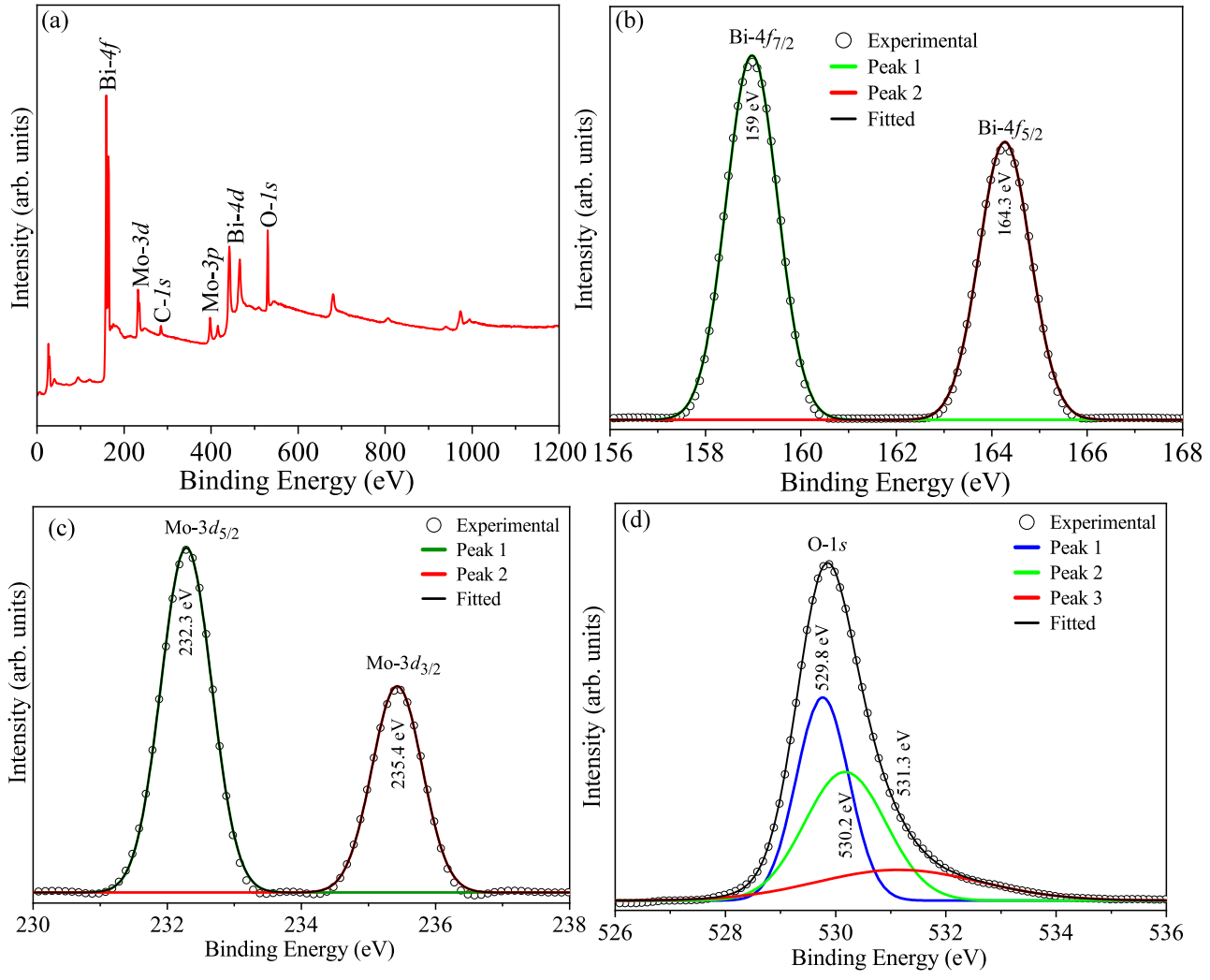

Figure 7. (a) XPS full survey and core level XPS spectra of (b) Bi-4f, (c) Mo-3d, and (d) O-1s for BMO-9.

https://doi.org/10.1021/acsomega.4c03171
ACS Omega 2024, 9, 36314−36325

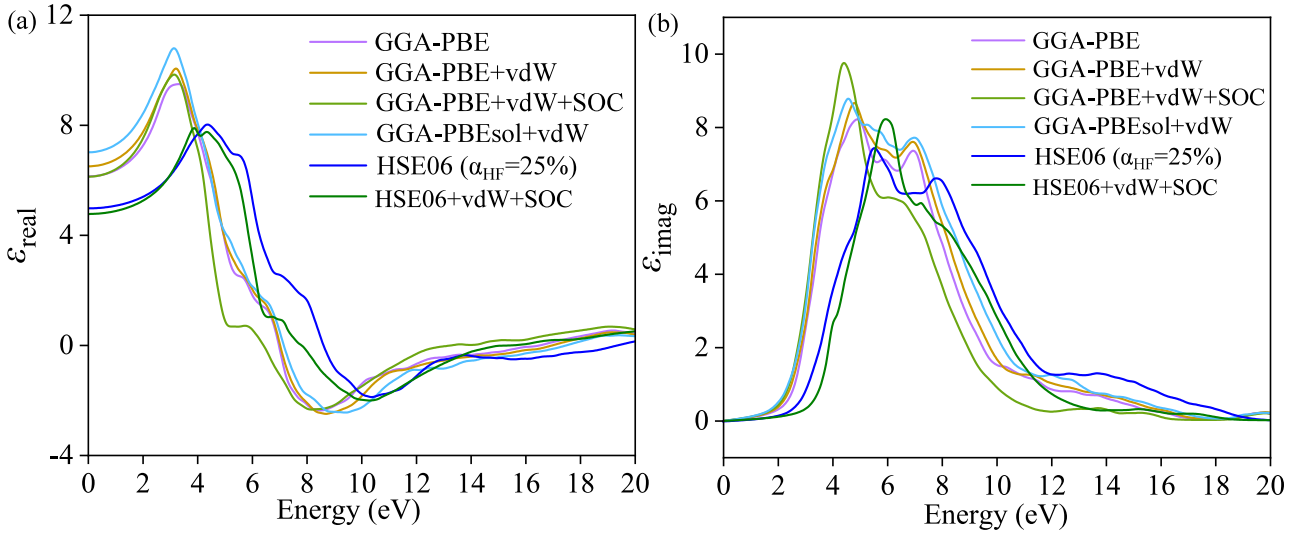

Figure 8. Linear optical response of BMO in terms of the (a) real part of dielectric constant ε_{real} and (b) imaginary part of the dielectric constant ε_{imag} as a function of photon energy calculated for GGA-PBE, GGA-PBE+vdW, GGA-PBE+vdW+SOC, GGA-PBEsol+vdW, HSE06 (α_{HF} = 25%), and HSE06+vdW+SOC averaged over three different polarizations E_x, E_y, and E_z.

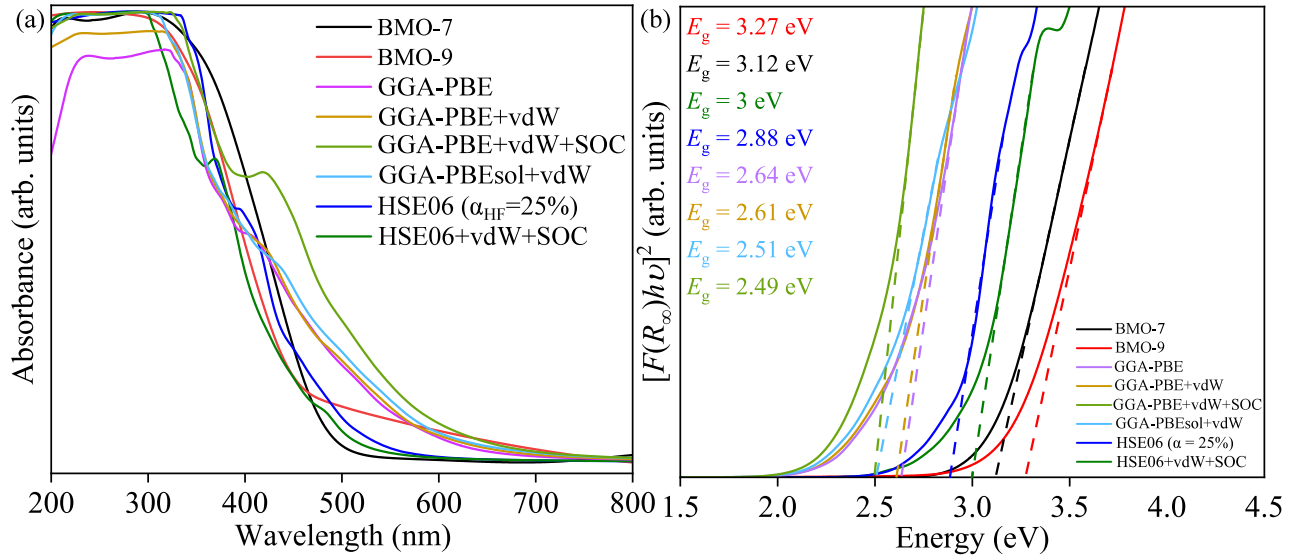

Figure 9. (a) Optical absorption and (b) corresponding Tauc plots of BMO-7 and BMO-9 derived from UV−vis diffuse absorption spectra were superimposed to that of GGA-PBE, GGA-PBE+vdW, GGA-PBE+vdW+SOC, GGA-PBEsol+vdW, HSE06 (α_{HF} = 25%), and HSE06+vdW+SOC.

xc functionals averaged over three polarization E_x, E_y, and E_z. In the static limit $\omega \to 0$, ε_{real} attained different values in the range of 4.8−7 for various functionals. The experimental value of zero frequency ε_{real} for BMO is not available for comparison. The ε_{imag} that encodes the optical absorption of the material is shown in Figure 8b. The energy threshold beyond which ε_{imag} increases rapidly shifted to the higher energy of ∼3 eV for the HSE06+vdW+SOC functional. The optical absorption $\alpha(\omega)$ can be derived from ε_{real} and ε_{imag} using the relation $\alpha(\omega) = \sqrt{2}\,\omega/c[\sqrt{\varepsilon_{real}^2(\omega) + \varepsilon_{imag}^2(\omega)} - \varepsilon_{real}(\omega)]$. In Figure 9a, the DFT-simulated absorptions for different xc functionals are superimposed on those of experimental observations obtained from DRS measurements using the Kubelka−Munk function $F(R_\infty)$. The simulated steep absorption edge for HSE06+vdW+SOC was located very close to the experimentally observed ones of both BMO-7 and BMO-9. The Tauc procedure following eq 3

$$[F(R_\infty)h\nu]^{1/\gamma} = A(h\nu - E_g) \tag{3}$$

was used to estimate the band gap E_g where A denotes a constant, h is for Planck's, ν represents photon frequency, and γ sets the electronic transition type (indirect γ = 2 and direct γ = 1/2). In the case of the γ = 1/2 direct transition, the value of A is defined by the index of refraction n, effective mass of electron m_e^* and hole m_h^*, speed of light c, and charge of electron q using the following relation:[94]

$$A \approx \frac{q^4\left[2\frac{m_e^* m_h^*}{m_e^* + m_h^*}\right]^3}{n^2 c^2 h^4 m_e^{*2}}\ \text{eV cm}^{-2} \tag{4}$$

The BMO is known to be a direct band gap material.[16,23,26,29,76,91,95] The onset of $[F(R_\infty)h\nu]^2$ versus the photon energy $E = h\nu$ in Tauc plots in Figure 9b bears the signature of the direct nature of the band gap. The intercepts of

https://doi.org/10.1021/acsomega.4c03171
ACS Omega 2024, 9, 36314−36325

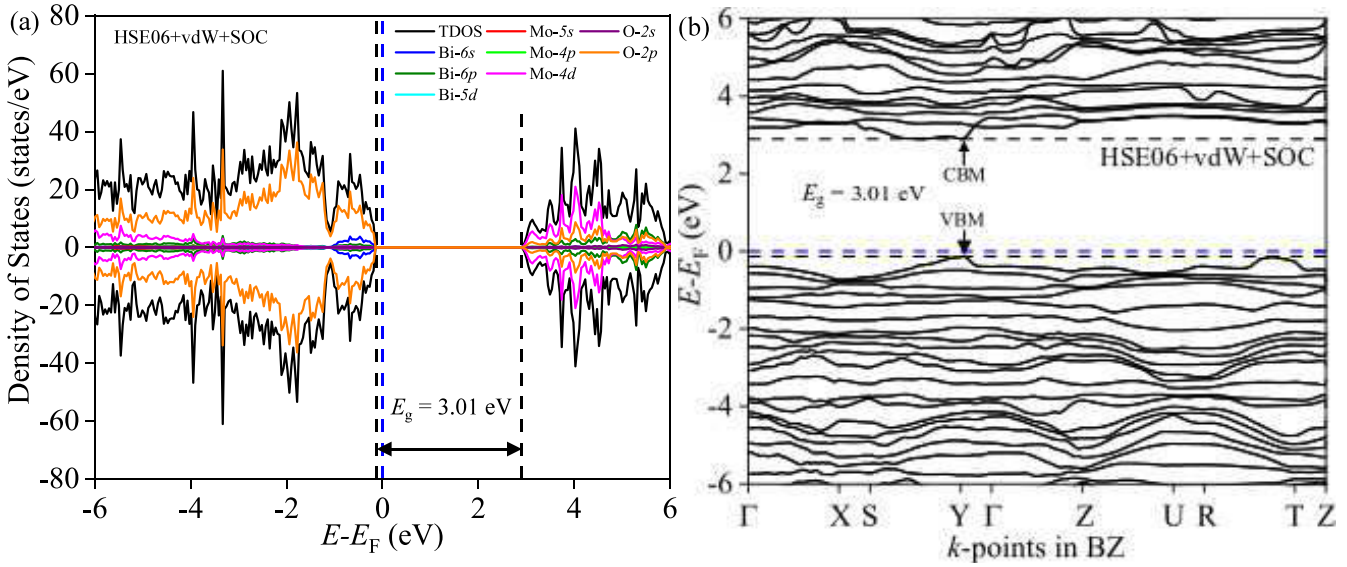

Figure 10. (a) Total density of states (TDOS) and its projections on different orbitals of Bi, Mo, and O atoms, and (b) electronic BS along the Γ, R, S, T, U, X, Y, and Z high symmetry points in BZ for HSE06+vdW+SOC.

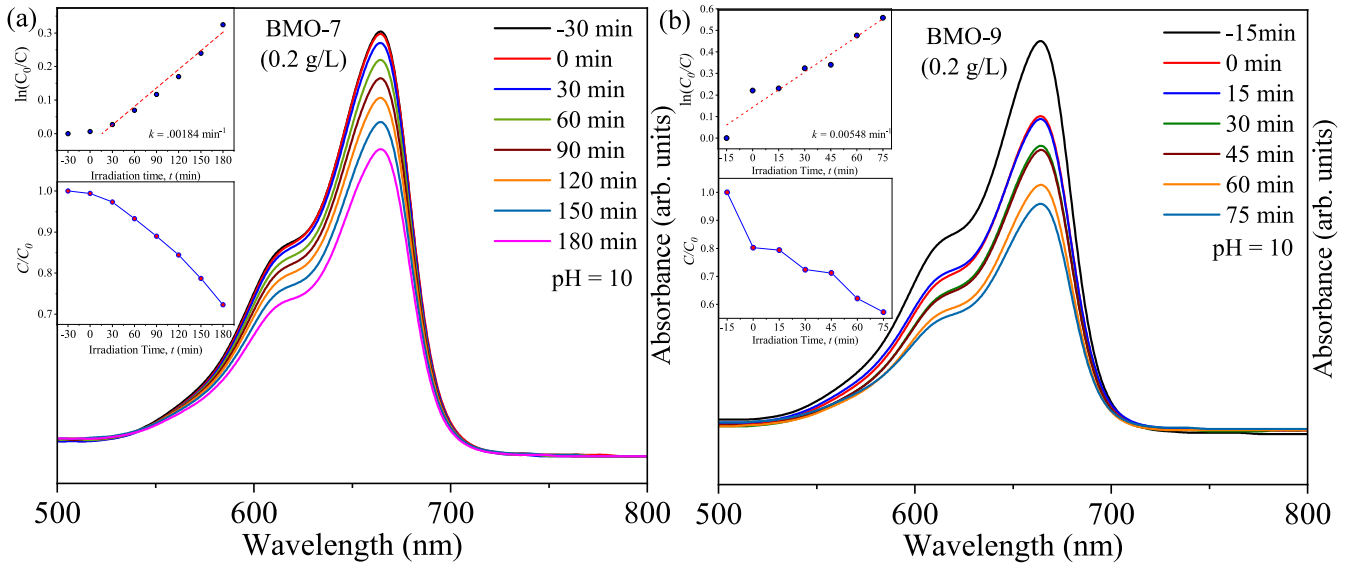

Figure 11. Photocatalytic degradation measurements from the UV−vis absorption spectra of the (a) BMO-7 and (b) BMO-9 photocatalysts (0.20 g/L) with 10 ppm MB dye.

extrapolation from the steepest edges on the energy axis revealed direct E_g values of 3.12 and 3.27 eV for BMO-7 and BMO-9, respectively. The underestimated E_g remained below 2.64 eV for nonhybrid xc functionals. The steep rising edges of Tauc plots shifted to a higher E_g value of 2.88 eV for hybrid HSE06. The vdW and SOC corrections in HSE06+vdW+SOC produced E_g = 3 eV, which agrees well with the experimental observation. The estimated value of A = 2083 eV cm^{-2} from HSE06+vdW+SOC lies close to that of the experimental 1562 (1493) eV cm^{-2} for BMO-7 (BMO-9).

3.8. Electronic Properties Analysis. For conciseness sake, the detailed total density of states (TDOS), its orbital projections (PDOS), along with BS for different functionals were presented in the Supporting Information. The GGA-PBE produced an underestimated E_g of 2 eV in Figure S3a. The vdW corrections as GGA-PBE+vdW in Figure S3b deteriorate the E_g underestimation to 1.83 eV. Moreover, incorporating SOC as GGA-PBE+vdW+SOC in Figure S3c has no appreciable effect on the DOS, and E_g remained ∼1.83 eV. The HSE06 with α_{HF} = 25% increased the E_g to 2.83 eV in Figure S3d, which is still an underestimation of the experimental E_g. The exchange-correlation energy E_{xc}^{HSE} for HSE06 is defined in terms of short-range (SR) and long-range (LR) components as

$$E_{xc}^{HSE} = \alpha_{HF}E_x^{HF,SR}(\mu) + (1 - \alpha_{HF})E_x^{PBE,SR}(\mu) + E_x^{PBE,LR}(\mu) + E_c^{PBE}(\mu) \quad (5)$$

where the screening parameter μ in hybrid functionals was set to 0.2 Å^{-1}.[96,97] Although HSE06 (μ = 0.2 Å^{-1}, α_{HF} = 25%) described many semiconductor oxides E_g with good accuracy, the observed underestimation can be ascribed to the wide band gap nature of BMO.[98,99] The vdW corrections in HSE06+vdW provide a minor increment in E_g to 2.89 eV; see Figure S3e.

https://doi.org/10.1021/acsomega.4c03171
ACS Omega 2024, 9, 36314−36325

The orbital compositions of the DOS remained invariant across different functionals. The bonding states near the valence band maxima (VBM) stemmed from the hybridization of the Bi6s, Mo-4p, and O-2p orbitals. The antibonding states at conduction band minima (CBM) germinated from orbital hybridization among the Bi6p, Mo-4d, and O-2p orbitals. The corresponding electronic BSs simulated from different functionals are shown in Figure S4a−e. The estimated E_g values from the BS and DOS differ by $\lesssim$0.25 eV for GGA-PBE (2.25 eV), GGA-PBE+vdW (2 eV), GGA-PBE+vdW+SOC (2 eV), HSE06 (3.06 eV), and HSE06+vdW (3 eV). For most of the xc approximations, the incorrect indirect nature of the electronic band gap was evident as VBM stayed at Γ while the CBM was shifted to X → Γ except for the GGA-PBE, where the VBM and CMB are situated at the same Γ. The inclusion of SOC as HSE06+vdW+SOC in Figure 10a provided E_g = 3.01 eV, which was in good agreement with the experimentally observed E_g of 3.12 and 3.27 eV for BMO-7 and BMO-9, respectively. The corresponding electronic BS in Figure 10b revealed both VBM and CBM at the same k-point close to Y in the BZ, which preserved the expected direct nature of the band gap. The dense k-points-based BS simulation accurately resembled the E_g = 3.01 eV measured from the DOS.

Now we explore the potential of computationally cheap DFT+U_d+U_p in combination with the vdW corrections for explaining the electronic structure of BMO. Systematic tuning of U_d (on Bi-5d and Mo-4d) and U_p (Bi-6p and O-2p) was attempted to obtain the desired E_g as shown in Figures S5 and S6. The E_g underestimation persisted for all (U_d, U_p) values with the vdW force turned on. The largest E_g of 2.41 eV was obtained by applying U_p as high as 15 eV on Bi-6p; see Figure S5f. The corresponding electronic BS in Figure S7f revealed E_g = 2.6 eV with the indirect nature of electronic transition due to incorrect energy dispersion. Without the vdW corrections, DFT+U_d+U_p produced a higher E_g of 2.56 eV (2.71 eV) in Figure S6f (Figure S8f) with incorrect indirect band gap and severe volume overestimation; see Table S1. In summary, the DFT+U_d+U_p+vdW approach was unsuccessful in modeling the experimentally obtained high E_g ($\gtrsim$3 eV) of BMO.

3.9. Photocatalytic Measurements. The photocatalytic degradation measurements of BMO-7 and BMO-9 were shown in Figure 11a,b. The diminishing absorption peak of MB at 665 nm indicates its degradation over time by photocatalytic means. No dye degradation in the dark condition was evident in Figure 11a for BMO-7. Yet in the case of BMO-9 in Figure 11b, dye degradation in the dark was present due to surface adsorption effects. The ratio C_0/C as a function of irradiation time t in the insets of Figure 11 was used to estimate the photocatalytic performances of the photocatalysts. The BMO-7 (BMO-9) sample annihilated the MB dye by 28% (43%) in 180 (75) min of irradiation. The pseudo-first-order model obtained the reaction rate k from $\ln(C_0/C) = kt$.[100,101] The estimated values of k were found to be 0.00184 and 0.00548 min^{-1} for BMO-7 and BMO-9, respectively.

4. CONCLUSION

We have presented comprehensive first-principles calculations on the physical properties of solvothermally synthesized $Pca2_1$ orthorhombic phase pure and wide band gap BMO. The mechanical stability of BMO was confirmed by correlating the elastic properties derived from the equation of state and elastic tensor simulations. The desired dynamical stability of BMO at T = 0 K was established by the absence of imaginary modes in phonon BS simulations based on the finite difference-based supercell method. The experimentally observed Raman and infrared absorptions of BMO were modeled from the simulated Raman tensor and phonon DOS, respectively. The optical absorption derived from the simulated complex dielectric constant using the HSE06+SOC+vdW functional corroborated the corresponding experimental observations. Moreover, the HSE06+SOC+vdW reliably produced the magnitude and the direct nature of the diffuse reflectance-based electronic band gap. The best photocatalytic efficiency of BMO was ∼43% in degrading MB dye under 75 min optical illumination. In summary, this combined experimental−theoretical approach may have successfully modeled the physical properties of BMO relevant to solar harvesting applications.

■ ASSOCIATED CONTENT

Data Availability Statement

The data presented in this study are contained within the Article and Supporting Information.

Supporting Information

The Supporting Information is available free of charge at https://pubs.acs.org/doi/10.1021/acsomega.4c03171.

Detailed experimental crystallographic parameters derived from Rietveld refinement of XRD and DFT-relaxed structures, elastic properties simulation, Raman, and FTIR peak assignments with DFT simulations, phonon density of states and band structure simulations, Born tensor simulations, EDX analysis, and DFT simulated electronic properties of γ-Bi_2MoO_6 (PDF)

■ AUTHOR INFORMATION

Corresponding Author

Imtiaz Ahmed − *Materials Science Research Laboratory, Department of Electrical and Electronic Engineering, University of Dhaka, Dhaka 1000, Bangladesh;* orcid.org/0000-0003-3997-1421; Email: imtiaz@du.ac.bd

Authors

Shahad Saroar − *Materials Science Research Laboratory, Department of Electrical and Electronic Engineering, University of Dhaka, Dhaka 1000, Bangladesh;* orcid.org/0009-0009-6608-6293

Shadmin Sultana − *Materials Science Research Laboratory, Department of Electrical and Electronic Engineering, University of Dhaka, Dhaka 1000, Bangladesh*

Sadiq Shahriyar Nishat − *Department of Materials Science and Engineering, Rensselaer Polytechnic Institute, Troy, New York 12180, United States;* orcid.org/0000-0003-4236-346X

Quazi Shafayat Hossain − *Materials Science Research Laboratory, Department of Electrical and Electronic Engineering, University of Dhaka, Dhaka 1000, Bangladesh*

M. N. I. Khan − *Materials Science Division, Atomic Energy Centre, Dhaka 1000, Bangladesh*

Dipa Islam − *Biomedical and Toxicological Research Institute, Bangladesh Council of Scientific and Industrial Research, Dhaka 1205, Bangladesh*

Umme Sarmeen Akhtar − *Institute of Glass and Ceramic Research and Testing, Bangladesh Council of Scientific and*

https://doi.org/10.1021/acsomega.4c03171
ACS Omega 2024, 9, 36314−36325

Industrial Research, Dhaka 1205, Bangladesh; orcid.org/0000-0003-0659-8288

Muhammad Shahriar Bashar − *Institute of Energy Research and Development, Bangladesh Council of Scientific and Industrial Research, Dhaka 1205, Bangladesh*

Sharmin Jahan − *Institute of Food Science and Technology, Bangladesh Council of Scientific and Industrial Research, Dhaka 1205, Bangladesh*

Khandker Saadat Hossain − *Nanophysics and Soft Matter Laboratory, Department of Physics, University of Dhaka, Dhaka 1000, Bangladesh*

Complete contact information is available at: https://pubs.acs.org/10.1021/acsomega.4c03171

Author Contributions

I.A. planned and supervised the entire project and wrote the original article. S.Sa. and S.Su. contributed equally. S.Sa. and S.Su. synthesized the samples and performed all photocatalytic measurements. S.S.N., Q.S.H., S.Sa., S.Su., and I.A. performed the DFT simulations. M.N.I.K. helped with XRD and FTIR measurements. M.S.B. and S.J. facilitated the SEM, EDX, and Raman measurements. U.S.A. performed the XPS measurements. D.I. carried out the FESEM measurements. K.S.H. helped with optical measurements. S.Sa., S.Su., Q.S.H., and I.A. performed the data curation.

Notes

The authors declare no competing financial interest.

■ ACKNOWLEDGMENTS

I.A. gratefully acknowledges financial support from the University of Dhaka Research Fund 2023-24 for conducting this project. I.A. thankfully extends his courtesy to the Bangladesh Research and Education Network (BdREN) for providing excellent, high-performance computational resources. I.A. would like to thank the Semiconductor Technology Research Centre (STRC), University of Dhaka, for experimental support. I.A. also acknowledges resource-sharing support from Md. Shafiul Alam, University of Dhaka. I.A. would like to thank Shirin Akter Jahan, Institute of Glass and Ceramic Research and Testing (IGCRT), Bangladesh Council of Scientific and Industrial Research (BCSIR), regarding XPS measurements. K.S.H. acknowledges the support from the International Science Program (ISP), Uppsala University, Sweden.

■ REFERENCES

(1) Han, B.; Zhang, J.; Li, P.; Li, J.; Bian, Y.; Shi, H. Synthesis and luminescence properties of Eu^{3+} doped high temperature form of Bi_2MoO_6. *J. Electron. Mater.* **2015**, *44*, 1028.

(2) Zhou, D.; Wang, H.; Yao, X.; Pang, L.-X. Microwave dielectric properties of low temperature firing $Bi_2Mo_2O_9$ ceramic. *J. Am. Ceram. Soc.* **2008**, *91*, 3419.

(3) Wu, K.; Chai, H.; Xu, K.; Debliquy, M.; Zhang, C. Effect of 010 crystal facets of Bi_2MoO_6 and 1D/2D heterostructures for conductometric room temperature NH_3 gas sensors. *Sens. Actuators B: Chem.* **2023**, *376*, 132983.

(4) Kulkarni, A. K.; Tamboli, M. S.; Nadargi, D. Y.; Sethi, Y. A.; Suryavanshi, S. S.; Ghule, A. V.; Kale, B. B. Bismuth molybdate (α-$Bi_2Mo_3O_{12}$) nanoplates via facile hydrothermal and its gas sensing study. *J. Solid State Chem.* **2020**, *281*, 121043.

(5) Seevakan, K.; Manikandan, A.; Devendran, P.; Slimani, Y.; Baykal, A.; Structural, T. magnetic and electrochemical characterizations of $Bi_2Mo_2O_9$ nanoparticle for supercapacitor application. *J. Magn. Magn. Mater.* **2019**, *486*, 165254.

(6) Shetty, M.; Murthy, M.; Shastri, M.; Sindhusree, M.; Nagaswarupa, H.; Shivaramu, P. D.; Rangappa, D. Hydrothermally synthesized Bi_2MoO_6/Reduced Graphene Oxide composite as anodes for lithium-ion batteries. *Ceram. Int.* **2019**, *45*, 24965.

(7) Zhao, Y.; Yi, G.; Kang, W.; Hou, Q.; Xing, B.; Huang, G.; Dong, H.; Zhang, C.; Zhang, Y. N-doped carbon dots modified Bi_2MoO_6 microspheres as anode materials for high performance aqueous rechargeable nickel/bismuth batteries. *Appl. Surf. Sci.* **2023**, *614*, 156191.

(8) Wu, L.; Hu, J.; Sun, C.; Jiao, F. Construction of Z-scheme CoAl-LDH/Bi_2MoO_6 heterojunction for enhanced photocatalytic degradation of antibiotics in natural water bodies. *Process Saf. Environ. Prot.* **2022**, *168*, 1109.

(9) Rodríguez-Girón, J.; Hernández-Uresti, D.; Obregón, S.; Juárez-Ramírez, I.; Sánchez-Martínez, D. One-step microwave-assisted hydrothermal synthesis of α-$Bi_2Mo_3O_{12}$ without surfactants at low temperature for their application in tetracycline photodegradation. *Mater. Today Commun.* **2022**, *33*, 104695.

(10) He, R.; Xu, D.; Cheng, B.; Yu, J.; Ho, W. Review on nanoscale Bi-based photocatalysts. *Nanoscale Horiz.* **2018**, *3*, 464.

(11) Wu, X.; Ng, Y. H.; Wen, X.; Chung, H. Y.; Wong, R. J.; Du, Y.; Dou, S. X.; Amal, R.; Scott, J. Construction of a Bi_2MoO_6: $Bi_2Mo_3O_{12}$ heterojunction for efficient photocatalytic oxygen evolution. *Chem. Eng. J.* **2018**, *353*, 636.

(12) Ono, T.; Utsumi, K.; Tsukamoto, S.; Tamaru, H.; Kataoka, M.; Noguchi, F. Roles of bulk γ (L)-Bi_2MoO_6 and surface β-$Bi_2Mo_2O_9$ in the selective catalytic oxidation of C_3H_6. *J. Mol. Catal. A-Chem.* **2010**, *318*, 94.

(13) Le Bahers, T.; Rerat, M.; Sautet, P. Semiconductors used in photovoltaic and photocatalytic devices: Assessing fundamental properties from DFT. *J. Phys. Chem. C* **2014**, *118*, 5997.

(14) Guo, C.; Xu, J.; Wang, S.; Li, L.; Zhang, Y.; Li, X. Facile synthesis and photocatalytic application of hierarchical mesoporous Bi_2MoO_6 nanosheet-based microspheres. *CrystEngComm* **2012**, *14*, 3602.

(15) Ren, J.; Wang, W.; Shang, M.; Sun, S.; Gao, E. Heterostructured bismuth molybdate composite: preparation and improved photocatalytic activity under visible-light irradiation. *ACS Appl. Mater. Interfaces* **2011**, *3*, 2529.

(16) Zhang, M.; Shao, C.; Zhang, P.; Su, C.; Zhang, X.; Liang, P.; Sun, Y.; Liu, Y. Bi_2MoO_6 microtubes: controlled fabrication by using electrospun polyacrylonitrile microfibers as template and their enhanced visible light photocatalytic activity. *J. Hazard. Mater.* **2012**, *225*, 155.

(17) Getsoian, A. B.; Shapovalov, V.; Bell, A. T. DFT+*U* investigation of propene oxidation over bismuth molybdate: active sites, reaction intermediates, and the role of bismuth. *J. Phys. Chem. C* **2013**, *117*, 7123.

(18) Yu, R.; Fan, A.; Yuan, M.; Li, T.; Wang, J. Observation of intrinsic emission in β-$BiNbO_4$ available for excitation of both UV light and high energy irradiation. *Phys. Chem. Chem. Phys.* **2016**, *18*, 23702.

(19) Sun, Q.; Wang, J.; Yin, W.-J.; Yan, Y. Bandgap Engineering of Stable Lead-Free Oxide Double Perovskites for Photovoltaics. *Adv. Mater.* **2018**, *30*, 1705901.

(20) Tiwari, D.; Alibhai, D.; Cherns, D.; Fermin, D. J. Crystal and Electronic Structure of Bismuth Thiophosphate, $BiPS_4$: An Earth-Abundant Solar Absorber. *Chem. Mater.* **2020**, *32*, 1235.

(21) Yoshii, K.; Fukuda, T.; Akahama, H.; Kano, J.; Kambe, T.; Ikeda, N. Magnetic and dielectric study of Bi_2CuO_4. *Phys. C: Supercond. Appl.* **2011**, *471*, 766.

(22) Hao, Y.; Dong, X.; Wang, X.; Ma, H.; Zhang, X. Ultrathin-nanosheet-assembled Bi_2MoO_6 mesoporous hollow framework for realizing optimized sunlight-driven photocatalytic water oxidation. *RSC Adv.* **2016**, *6*, 102155.

(23) Dutta, D. P.; Ballal, A.; Chopade, S.; Kumar, A. A study on the effect of transition metal (Ti^{4+}, Mn^{2+}, Cu^{2+} and Zn^{2+})-doping on visible light photocatalytic activity of Bi_2MoO_6 nanorods. *J. Photochem. Photobiol. A: Chem.* **2017**, *346*, 105.

(24) Kumar, R.; Sudhaik, A.; Raizada, P.; Hosseini-Bandegharaei, A.; Thakur, V. K.; Saini, A.; Saini, V.; Singh, P. An overview on bismuth molybdate based photocatalytic systems: Controlled morphology and enhancement strategies for photocatalytic water purification. *J. Environ. Chem. Eng.* **2020**, *8*, 104291.
(25) Peng, Y.; Zhang, Y.; Tian, F.; Zhang, J.; Yu, J. Structure tuning of Bi_2MoO_6 and their enhanced visible light photocatalytic performances. *Crit. Rev. Solid State Mater. Sci.* **2017**, *42*, 347.
(26) Bi, J.; Che, J.; Wu, L.; Liu, M. Effects of the solvent on the structure, morphology and photocatalytic properties of Bi_2MoO_6 in the solvothermal process. *Mater. Res. Bull.* **2013**, *48*, 2071.
(27) Kongmark, C.; Coulter, R.; Cristol, S.; Rubbens, A.; Pirovano, C.; Lofberg, A.; Sankar, G.; van Beek, W.; Bordes-Richard, E.; Vannier, R.-N. A comprehensive scenario of the crystal growth of γ-Bi_2MoO_6 catalyst during hydrothermal synthesis. *Cryst. Growth Des.* **2012**, *12*, 5994.
(28) Martınez-de la Cruz, A.; Obregon Alfaro, S. Synthesis and characterization of γ-Bi_2MoO_6 prepared by coprecipitation: photo-assisted degradation of organic dyes under vis-irradiation. *J. Mol. Catal. A-Chem.* **2010**, *320*, 85.
(29) Li, H.; Li, W.; Gu, S.; Wang, F.; Liu, X.; Ren, C. Forming oxygen vacancies inside in lutetium-doped Bi_2MoO_6 nanosheets for enhanced visible-light photocatalytic activity. *Mol. Catal.* **2017**, *433*, 301.
(30) Núñez-González, R.; Rangel, R.; Antúnez-García, J.; Galván, D. H. DFT study of electronic structure and optical properties of Ru-doped low-temperature γ-Bi_2MoO_6 phase. *Solid State Commun.* **2020**, *318*, 113978.
(31) Zhang, B.; Liu, G.; Shi, H.; Wu, Q.; Xue, S.; Shao, T.; Zhang, F.; Liu, X. Density Functional Theory Study of Electronic Structure and Optical Properties of Ln^{3+}-Doped γ-Bi_2MoO_6 (Ln= Gd, Ho, Yb). *Crystals* **2023**, *13*, 1158.
(32) Hossain, M. Z.; Nishat, S. S.; Ahmed, S.; Hossain, Q. S.; Khan, M. N.; Hasan, T.; Bashar, M. S.; Faysal, A. S. H.; Syed, I. M.; Hossain, K. S.; et al. Combined experimental and DFT approach to $BiNbO_4$ polymorphs. *RSC Adv.* **2023**, *13*, 5576.
(33) Hossain, Q. S.; Ahmed, S.; Nishat, S. S.; Hossain, M. Z.; Khan, M. N. I.; Hasan, T.; Bashar, M. S.; Hakim, M.; Syed, I. M.; Hossain, K. S.; et al. An ab initio DFT perspective on experimentally synthesized $CuBi_2O_4$. *RSC Adv.* **2023**, *13*, 14291.
(34) Fardush Tanha, J.; Farhad, S.; Honey, U.; Tanvir, N.; Hasan, T.; Shahriyar Nishat, S.; Kabir, A.; Ahmed, S.; Hakim, M.; Khan, M. N. I.; et al. A DFT+*U* look into experimentally synthesized monoclinic scheelite $BiVO_4$. *J. Appl. Phys.* **2021**, *130*, 235107.
(35) Ahmed, S.; Nishat, S. S.; Kabir, A.; Faysal, A. S. H.; Hasan, T.; Chakraborty, S.; Ahmed, I. Structural, elastic, vibrational, electronic and optical properties of $SmFeO_3$ using density functional theory. *Physica B Condens. Matter.* **2021**, *615*, 413061.
(36) Ahmed, S.; Hasan, T.; Faysal, A. S. H.; Nishat, S. S.; Khan, M. N. I.; Kabir, A.; Ahmed, I. A DFT+*U* approach to doped $SrTiO_3$ for solar harvesting applications. *Comput. Mater. Sci.* **2022**, *214*, 111743.
(37) Hossain, Q. S.; Nishat, S. S.; Sultana, M.; Mahi, T. A.; Ahmed, S.; Khan, M. N. I.; Das, H. N.; Bashar, M. S.; Akhtar, U. S.; Jahan, S.; et al. A combined first principles and experimental approach to Bi_2WO_6. *RSC Adv.* **2023**, *13*, 36130.
(38) Ma, X.; Lu, B.; Li, D.; Shi, R.; Pan, C.; Zhu, Y. Origin of photocatalytic activation of silver orthophosphate from first-principles. *J. Phys. Chem. C* **2011**, *115*, 4680.
(39) Park, H. S.; Kweon, K. E.; Ye, H.; Paek, E.; Hwang, G. S.; Bard, A. J. Factors in the metal doping of $BiVO_4$ for improved photoelectrocatalytic activity as studied by scanning electrochemical microscopy and first-principles density-functional calculation. *J. Phys. Chem. C* **2011**, *115*, 17870.
(40) Haq, M. R.; Ehsan, N.; Nishat, S. S.; Hossain, Q. S.; Khan, M. N. I.; Shahriar Bashar, M.; Akhtar, U. S.; Chowdhury, F.; Jahan, S.; Hossain, K. S.; et al. Comprehensive First-Principles Modeling of Experimentally Synthesized $BiPO_4$ Polymorphs. *J. Phys. Chem. C* **2024**, *128*, 4779.
(41) Kresse, G.; Furthmüller, J. Efficient iterative schemes for ab initio total-energy calculations using a plane-wave basis set. *Phys. Rev. B* **1996**, *54*, 11169.
(42) Kresse, G.; Joubert, D. From ultrasoft pseudopotentials to the projector augmented-wave method. *Phys. Rev. B* **1999**, *59*, 1758.
(43) Blöchl, P. E. Projector augmented-wave method. *Phys. Rev. B* **1994**, *50*, 17953.
(44) Jain, A.; Shin, Y.; Persson, K. A. Computational predictions of energy materials using density functional theory. *Nat. Rev. Mater.* **2016**, *1*, 1.
(45) Jones, R. O. Density functional theory: Its origins, rise to prominence, and future. *Rev. Mod. Phys.* **2015**, *87*, 897.
(46) Ceperley, D. M.; Alder, B. J. Ground state of the electron gas by a stochastic method. *Phys. Rev. Lett.* **1980**, *45*, 566.
(47) Perdew, J. P.; Burke, K.; Ernzerhof, M. Generalized gradient approximation made simple. *Phys. Rev. Lett.* **1996**, *77*, 3865.
(48) Perdew, J. P.; Ruzsinszky, A.; Csonka, G. I.; Vydrov, O. A.; Scuseria, G. E.; Constantin, L. A.; Zhou, X.; Burke, K. Restoring the density-gradient expansion for exchange in solids and surfaces. *Phys. Rev. Lett.* **2008**, *100*, 136406.
(49) Dudarev, S.; Botton, G.; Savrasov, S.; Humphreys, C.; Sutton, A. Electron-energy-loss spectra and the structural stability of nickel oxide: An LSDA+U study. *Phys. Rev. B* **1998**, *57*, 1505.
(50) Volnianska, O.; Boguslawski, P.; Kaczkowski, J.; Jakubas, P.; Jezierski, A.; Kaminska, E. Theory of doping properties of Ag acceptors in ZnO. *Phys. Rev. B* **2009**, *80*, 245212.
(51) Sheetz, R. M.; Ponomareva, I.; Richter, E.; Andriotis, A. N.; Menon, M. Defect-induced optical absorption in the visible range in ZnO nanowires. *Phys. Rev. B* **2009**, *80*, 195314.
(52) Lathiotakis, N. N.; Andriotis, A. N.; Menon, M. Codoping: A possible pathway for inducing ferromagnetism in ZnO. *Phys. Rev. B* **2008**, *78*, 193311.
(53) Park, S.-G.; Magyari-K̈ope, B.; Nishi, Y. Electronic correlation effects in reduced rutile TiO_2 within the LDA+*U* method. *Phys. Rev. B* **2010**, *82*, 115109.
(54) Heyd, J.; Scuseria, G. E.; Ernzerhof, M. Hybrid functionals based on a screened Coulomb potential. *J. Chem. Phys.* **2003**, *118*, 8207.
(55) Franchini, C. Hybrid functionals applied to perovskites. *J. Phys.: Condens. Matter* **2014**, *26*, 253202.
(56) Stroppa, A.; Kresse, G. Unraveling the Jahn-Teller effect in Mn-doped GaN using the Heyd-Scuseria-Ernzerhof hybrid functional. *Phys. Rev. B* **2009**, *79*, 201201.
(57) Stroppa, A.; Picozzi, S. Hybrid functional study of proper and improper multiferroics. *Phys. Chem. Chem. Phys.* **2010**, *12*, 5405.
(58) Marsman, M.; Paier, J.; Stroppa, A.; Kresse, G. Hybrid functionals applied to extended systems. *J. Phys.: Condens. Matter* **2008**, *20*, 064201.
(59) Grimme, S.; Ehrlich, S.; Goerigk, L. Effect of the damping function in dispersion corrected density functional theory. *J. Comput. Chem.* **2011**, *32*, 1456.
(60) Weng, B.; Xiao, Z.; Meng, W.; Grice, C. R.; Poudel, T.; Deng, X.; Yan, Y. Bandgap engineering of barium bismuth niobate double perovskite for photoelectrochemical water oxidation. *Adv. Energy Mater.* **2017**, *7*, 1602260 DOI: 10.1002/aenm.201602260.
(61) Baroni, S.; De Gironcoli, S.; Dal Corso, A.; Giannozzi, P. Phonons and related crystal properties from density-functional perturbation theory. *Rev. Mod. Phys.* **2001**, *73*, 515.
(62) Giustino, F. Electron-phonon interactions from first principles. *Rev. Mod. Phys.* **2017**, *89*, 015003.
(63) Togo, A.; Tanaka, I. First principles phonon calculations in materials science. *Scr. Mater.* **2015**, *108*, 1.
(64) Togo, A.; Chaput, L.; Tadano, T.; Tanaka, I. Implementation strategies in phonopy and phono3py. *J. Phys.: Condens. Matter* **2023**, *35*, 353001.
(65) Mostofi, A. A.; Yates, J. R.; Lee, Y.-S.; Souza, I.; Vanderbilt, D.; Marzari, N. wannier90: A tool for obtaining maximally-localised Wannier functions. *Comput. Phys. Commun.* **2008**, *178*, 685.

https://doi.org/10.1021/acsomega.4c03171
ACS Omega 2024, 9, 36314−36325

(66) Hou, Y.; Ardo, S.; Wu, R. Hybrid density functional study of band gap engineering of $SrTiO_3$ photocatalyst via doping for water splitting. *Phys. Rev. Mater.* **2021**, *5*, 065801.
(67) Giannozzi, P.; Baroni, S.; Bonini, N.; Calandra, M.; Car, R.; Cavazzoni, C.; Ceresoli, D.; Chiarotti, G. L.; Cococcioni, M.; Dabo, I.; et al. QUANTUM ESPRESSO: A modular and open-source software project for quantum simulations of materials. *J. Phys.: Condens. Matter.* **2009**, *21*, 395502.
(68) Giannozzi, P.; Andreussi, O.; Brumme, T.; Bunau, O.; Nardelli, M. B.; Calandra, M.; Car, R.; Cavazzoni, C.; Ceresoli, D.; Cococcioni, M.; et al. Advanced capabilities for materials modelling with Quantum ESPRESSO. *J. Phys.: Condens. Matter* **2017**, *29*, 465901.
(69) Giannozzi, P.; Baseggio, O.; Bonfa, P.; Brunato, D.; Car, R.; Carnimeo, I.; Cavazzoni, C.; De Gironcoli, S.; Delugas, P.; Ferrari Ruffino, F.; et al. Quantum ESPRESSO toward the exascale. *J. Chem. Phys.* **2020**, *152*, 154105.
(70) Bachelet, G. B.; Hamann, D. R.; Schlüter, M. Pseudopotentials that work: From H to Pu. *Phys. Rev. B* **1982**, *26*, 4199.
(71) Bettega, M.; Ferreira, L.; Lima, M. Transferability of local-density norm-conserving pseudopotentials to electron-molecule-collision calculations. *Phys. Rev. A* **1993**, *47*, 1111.
(72) Kresse, G.; Hafner, J. Norm-conserving and ultrasoft pseudopotentials for first-row and transition elements. *J. Condens. Matter Phys.* **1994**, *6*, 8245.
(73) Yu, C.; Viola, G.; Zhang, D.; Stroscio, Z.; Hu, Z.; Eskilla, V. R.; Grasso, S.; Wilson, R. M.; Zhou, K.; Bonini, N.; et al. Structural Evolution in $BiNbO_4$. *Inorg. Chem.* **2021**, *60*, 8507.
(74) Prosandeev, S.; Waghmare, U.; Levin, I.; Maslar, J. First-order Raman spectra of AB 1̀2B 1̀2O_3 double perovskites. *Phys. Rev. B* **2005**, *71*, 214307.
(75) Liu, Z.; Song, Y.; Wang, Q.; Jia, Y.; Tan, X.; Du, X.; Gao, S. Solvothermal fabrication and construction of highly photoelectrocatalytic TiO_2 NTs/Bi_2MoO_6 heterojunction based on titanium mesh. *J. Colloid Interface Sci.* **2019**, *556*, 92.
(76) Yang, Z.; Shen, M.; Dai, K.; Zhang, X.; Chen, H. Controllable synthesis of Bi_2MoO_6 nanosheets and their facet-dependent visible-light-driven photocatalytic activity. *Appl. Surf. Sci.* **2018**, *430*, 505.
(77) Xiao, H.; Tahir-Kheli, J.; Goddard, W. A., III Accurate band gaps for semiconductors from density functional theory. *J. Phys. Chem. Lett.* **2011**, *2*, 212.
(78) Csonka, G. I.; Perdew, J. P.; Ruzsinszky, A.; Philipsen, P. H.; Lebegue, S.; Paier, J.; Vydrov, O. A.; ´Angyán, J. G. Assessing the performance of recent density functionals for bulk solids. *Phys. Rev. B* **2009**, *79*, 155107.
(79) Birch, F. Finite strain isotherm and velocities for single-crystal and polycrystalline NaCl at high pressures and 300 K. *J. Geophys. Res. Solid Earth* **1978**, *83*, 1257.
(80) Ouahrani, T.; Garg, A. B.; Rao, R.; Rodriguez-Hernandez, P.; Munoz, A.; Badawi, M.; Errandonea, D. High-pressure properties of wolframite-type $ScNbO_4$. *J. Phys. Chem. C* **2022**, *126*, 4664.
(81) Wu, X.; Vanderbilt, D.; Hamann, D. Systematic treatment of displacements, strains, and electric fields in density-functional perturbation theory. *Phys. Rev. B* **2005**, *72*, 035105.
(82) Shang, S.; Wang, Y.; Liu, Z.-K. First-principles elastic constants of α and θ Al_2O_3. *Appl. Phys. Lett.* **2007**, *90*, 101909.
(83) Mouhat, F.; Coudert, F.-X. Necessary and sufficient elastic stability conditions in various crystal systems. *Phys. Rev. B* **2014**, *90*, 224104.
(84) Hill, R. The elastic behaviour of a crystalline aggregate. *Proc. Phys. Soc. A* **1952**, *65*, 349.
(85) Dong, H.; Chen, C.; Wang, S.; Duan, W.; Li, J. Elastic properties of tetragonal $BiFeO_3$ from first-principles calculations. *Appl. Phys. Lett.* **2013**, *102*, 182905.
(86) Yaakob, M.; Taib, M.; Deni, M.; Chandra, A.; Lu, L.; Yahya, M. First principle study on structural, elastic and electronic properties of cubic $BiFeO_3$. *Ceram. Int.* **2013**, *39*, S283.
(87) Maczka, M.; Hanuza, J.; Paraguassu, W.; Gomes Souza Filho, A.; Tarso Cavalcante Freire, P.; Mendes Filho, J. Phonons in ferroelectric Bi_2WO_6: Raman and infrared spectra and lattice dynamics. *Appl. Phys. Lett.* **2008**, *92*, 112911 DOI: 10.1063/1.2896312.
(88) Maczka, M.; Macalik, L.; Hermanowicz, K.; Kepiński, L.; Hanuza, J. Synthesis and phonon properties of nanosized Aurivillius phase of Bi_2MoO_6. *J. Raman Spectrosc.* **2010**, *41*, 1289.
(89) Graves, P.; Hua, G.; Myhra, S.; Thompson, J. The Raman modes of the Aurivillius phases: temperature and polarization dependence. *J. Solid State Chem.* **1995**, *114*, 112.
(90) Withers, R.; Thompson, J.; Rae, A. The crystal chemistry underlying ferroelectricity in $Bi_4Ti_3O_{12}$, Bi_3TiNbO_9, and Bi_2WO_6. *J. Solid State Chem.* **1991**, *94*, 404.
(91) Zhang, L.; Xu, T.; Zhao, X.; Zhu, Y. Controllable synthesis of Bi_2MoO_6 and effect of morphology and variation in local structure on photocatalytic activities. *Appl. Catal., B* **2010**, *98*, 138.
(92) Han, W.; Wu, T.; Wu, Q. Fabrication of WO_3/Bi_2MoO_6 heterostructures with efficient and highly selective photocatalytic degradation of tetracycline hydrochloride. *J. Colloid Interface Sci.* **2021**, *602*, 544.
(93) Zhu, X.-H.; Xiao, X.-B.; Chen, X.-R.; Liu, B.-G. Electronic structure, magnetism and optical properties of orthorhombic $GdFeO_3$ from first principles. *RSC Adv.* **2017**, *7*, 4054.
(94) Pankove, J. I. *Optical Processes in Semiconductors*; Dover Publications: Mineola, NY, 1975; pp 35−36.
(95) Shen, Y.; Huang, M.; Huang, Y.; Lin, J.; Wu, J. The synthesis of bismuth vanadate powders and their photocatalytic properties under visible light irradiation. *J. Alloys Compd.* **2010**, *496*, 287.
(96) Kweon, K. E.; Hwang, G. S. Structural phase-dependent hole localization and transport in bismuth vanadate. *Phys. Rev. B* **2013**, *87*, 205202.
(97) Schimka, L.; Harl, J.; Kresse, G. Improved hybrid functional for solids: The HSEsol functional. *J. Chem. Phys.* **2011**, *134*, 024116 DOI: 10.1063/1.3524336.
(98) Déak, P.; Duy Ho, Q.; Seemann, F.; Aradi, B.; Lorke, M. T. Choosing the correct hybrid for defect calculations: A case study on intrinsic carrier trapping in $\beta - Ga_2O_3$. *Phys. Rev. B* **2017**, *95*, 075208.
(99) Deák, P.; Lorke, M.; Aradi, B.; Frauenheim, T. Carbon in GaN: Calculations with an optimized hybrid functional. *Phys. Rev. B* **2019**, *99*, 085206.
(100) Sabuj, I. H.; Jahan, S. A.; Khan, M. N. I.; Akhtar, U. S.; Islam, D.; Bashar, M. S.; Das, H.; Jahan, S.; Hossain, Q. S.; Hossain, K. S.; et al. An experimental Look into efficient quaternary Bi_5O_7I/$Bi(IO_3)_3$/$Bi_2(IO_4)(IO_3)_3$/$BiOIO_3$ Photocatalytic Composite. *AIP. Adv.* **2024**, *14*, 035146.
(101) Mahi, T. A.; Hossain, Q. S.; Nishat, S. S.; Ahmed, S.; Khan, M.; Bashar, M. S.; Jahan, S. A.; Akhtar, U. S.; Jahan, S.; Chowdhury, F. A Combined Experimental and First Principles Look into (Ce, Mo) Doped $BiVO_4$. *Heliyon* **2024**, *10*, e29408.